



UvA-DARE (Digital Academic Repository)

A Deficit of Massive White Dwarfs in Gaia Astrometric Binaries

Hallakoun, N.; Shahaf, S.; Mazeh, T.; Toonen, S.; Ben-Ami, S.

DOI

[10.3847/2041-8213/ad5e63](https://doi.org/10.3847/2041-8213/ad5e63)

Publication date

2024

Document Version

Final published version

Published in

Astrophysical Journal Letters

License

CC BY

[Link to publication](#)

Citation for published version (APA):

Hallakoun, N., Shahaf, S., Mazeh, T., Toonen, S., & Ben-Ami, S. (2024). A Deficit of Massive White Dwarfs in Gaia Astrometric Binaries. *Astrophysical Journal Letters*, 970(1), Article L11. <https://doi.org/10.3847/2041-8213/ad5e63>

General rights

It is not permitted to download or to forward/distribute the text or part of it without the consent of the author(s) and/or copyright holder(s), other than for strictly personal, individual use, unless the work is under an open content license (like Creative Commons).

Disclaimer/Complaints regulations

If you believe that digital publication of certain material infringes any of your rights or (privacy) interests, please let the Library know, stating your reasons. In case of a legitimate complaint, the Library will make the material inaccessible and/or remove it from the website. Please Ask the Library: <https://uba.uva.nl/en/contact>, or a letter to: Library of the University of Amsterdam, Secretariat, P.O. Box 19185, 1000 GD Amsterdam, The Netherlands. You will be contacted as soon as possible.



A Deficit of Massive White Dwarfs in Gaia Astrometric Binaries

Na'ama Hallakoun¹ , Sahar Shahaf¹ , Tsevi Mazeh² , Silvia Toonen³ , and Sagi Ben-Ami¹ ¹Department of Particle Physics and Astrophysics, Weizmann Institute of Science, Rehovot 7610001, Israel; naama.hallakoun@weizmann.ac.il²School of Physics and Astronomy, Tel-Aviv University, Tel-Aviv 6997801, Israel³Anton Pannekoek Institute for Astronomy, University of Amsterdam, 1090 GE Amsterdam, The Netherlands

Received 2023 November 26; revised 2024 June 10; accepted 2024 July 2; published 2024 July 16

Abstract

The third data release of Gaia introduced a large catalog of astrometric binaries, out of which about 3200 are likely main-sequence stars with a white dwarf (WD) companion. These binaries are typically found with orbital separations of ~ 1 au, a separation range that was largely unexplored due to observational challenges. Such systems are likely to have undergone a phase of stable mass transfer while the WD progenitor was on the asymptotic giant branch. Here we study the WD mass distribution of a volume-complete sample of binaries with K/M dwarf primaries and orbital separations of ~ 1 au. We find that the number of massive WDs relative to the total number of WDs in these systems is smaller by an order of magnitude compared to their occurrence among single WDs in the field. One possible reason can be an implicit selection of the WD mass range if these are indeed post-stable-mass-transfer systems. Another reason can be the lack of merger products in our sample compared to the field, due to the relatively tight orbital separations of these systems. In addition, we find that about 14% of these systems have distant tertiary companions within 1 pc.

Unified Astronomy Thesaurus concepts: [White dwarf stars \(1799\)](#); [Astrometric binary stars \(79\)](#); [Post-asymptotic giant branch stars \(2121\)](#); [Multiple star evolution \(2153\)](#); [Gaia \(2360\)](#); [Interacting binary stars \(801\)](#); [Stellar mergers \(2157\)](#)

Materials only available in the [online version of record](#): machine-readable table

1. Introduction

Although the vast majority ($\gtrsim 97\%$; Althaus et al. 2010) of all stars end their lives as white dwarfs (WDs), the details of some of the most basic properties of their population are still far from consensus. Perhaps the most basic of all is the WD mass distribution, which bears the imprints of the initial mass function, the star formation history, and the stellar evolution (and in particular the initial-to-final mass relation) of both single and multiple stars.

The most prevalent technique for assessing the masses of WDs involves the fitting of their observed spectroscopic (e.g., Kepler et al. 2015, 2016, 2019) and/or photometric (e.g., Kilic et al. 2020; Jiménez-Esteban et al. 2023) data with theoretical atmospheric models. This fitting process yields the effective temperature and surface gravity of the WD, which can then be converted to mass using theoretical mass–radius relations or using the estimated radius if the parallax is known. While highly useful and applicable to many WDs, this approach is reliant on theoretical models and, as a result, may be susceptible to systematic errors stemming from potential inaccuracies within these models, such as the exact chemical composition of the WD atmosphere (e.g., Bergeron et al. 2019). It can also cause problems with low-resolution spectroscopy in the presence of strong magnetic fields (that are more common among massive WDs; e.g., García-Berro et al. 2016), due to absorption-line broadening by Zeeman splitting. Spectroscopic fitting is also problematic in the case of DC-type WDs, which show no absorption lines (e.g., Caron et al. 2023).

Other techniques for measuring WD masses that do not rely on atmospheric models, such as pulsational-mode analysis

(e.g., Córscico et al. 2019) and measuring the gravitational redshift of absorption lines (e.g., Falcon et al. 2010, 2012), are only applicable to a small number of WDs. Model-independent masses can also be obtained for WDs in astrometric binary systems (e.g., Gatewood & Gatewood 1978). Such systems were scarce until very recently, as will be discussed below.

In the absence of nuclear fusion, WDs slowly cool over billions of years. The more massive WDs become cooler and fainter sooner after star formation due to their much shorter progenitor main-sequence (MS) lifetimes (if they are formed through single-star evolution) and earlier onset of core crystallization, which significantly decreases their specific heat and accelerates their cooling rate (Fontaine et al. 2001). Cool WDs usually have faint absorption lines (if any), which are crucial for estimating their mass using atmospheric models. In addition, their smaller sizes make them intrinsically fainter than their lower-mass counterparts. For these reasons, magnitude-limited samples of WDs are biased against the more massive WDs ($\gtrsim 0.8 M_{\odot}$; e.g., Rebassa-Mansergas et al. 2015).

In order to derive the WD mass distribution, it is thus crucial to obtain a volume-limited unbiased census of WDs. With the exception of the nearly complete 20 pc WD sample (consisting of about 150 WDs; e.g., Toonen et al. 2017), the known WD sample in the pre-Gaia era was magnitude-limited rather than volume-limited and had been dominated by serendipitous discoveries and by targeted-yet-biased searches (such as searching for sources with ultraviolet excess; e.g., Green et al. 1986). The Sloan Digital Sky Survey (SDSS; York et al. 2000) successfully discovered a few tens of thousand WDs (e.g., Kepler et al. 2021), but the strong and largely unknown selection biases of the sample limited the possible statistical inferences.

It was not until the second data release of the Gaia space mission in 2018 (Gaia Collaboration et al. 2016, 2018) that a large, unbiased sample of WDs was compiled (Gentile Fusillo et al. 2019, and references therein). The Gaia catalog (along

with subsequent data releases; see Gaia Collaboration et al. 2021; Gentile Fusillo et al. 2021) allowed the construction of larger volume-limited samples, including the 20 pc (Hollands et al. 2018) and 40 pc (McCleery et al. 2020; Tremblay et al. 2020; O’Brien et al. 2023) samples, which are nearly complete for single WDs, and the 100 pc sample, which is considered to be nearly complete spectroscopically for single WDs down to an effective temperature of ~ 6000 K (i.e., still a magnitude-limited sample; see Jiménez-Esteban et al. 2018, 2023; Kilic et al. 2020).

The third data release (DR3) of Gaia (Gaia Collaboration et al. 2023b) was the first to include a catalog of unresolved sources with non-single-star solutions (Gaia Collaboration et al. 2023a). Recently, Shahaf et al. (2024) have identified nearly 3200 systems that are likely MS+WD binaries. This unprecedentedly large sample of WDs in solved astrometric binaries offers a unique opportunity to derive a model-independent mass distribution of a volume-complete WD sample. In this paper, we use this catalog to define volume-complete samples of MS+WD binaries with measured dynamical masses (Section 2). In Section 3, we compare the WD mass distribution of these samples with published mass distributions of field WDs within 100 pc, showing a stark deficit of massive WDs in our astrometric samples. Finally, in Section 4, we discuss several possible explanations for the observed difference between the distributions.

2. The Sample

2.1. The Astrometric Mass-ratio Function

In this paper, we use the Gaia DR3 catalog of unresolved sources with non-single-star solutions (Gaia Collaboration et al. 2023a). Since Gaia only detects the motion of the photocenter of the unresolved system, the nature of the companion(s) remains uncertain when it is based on the astrometric solution alone. Shahaf et al. (2019) introduced a triage method to rule out MS or binary-MS companions by defining a unitless observational parameter, named the “astrometric mass-ratio function” (AMRF):

$$\mathcal{A} \equiv \frac{\alpha_0}{\varpi} \left(\frac{M_1}{M_\odot} \right)^{-1/3} \left(\frac{P}{\text{yr}} \right)^{-2/3}, \quad (1)$$

where α_0 is the angular semimajor axis of the photocenter, ϖ is the parallax, P is the orbital period, and M_1 is the mass of the primary. This value can be calculated for every astrometric binary with a known M_1 , e.g., based on theoretical evolutionary tracks and the location on the Hertzsprung–Russell (H-R) diagram.

The measured AMRF values can then be compared to the expected AMRF values for a given combination of mass ratio, $q = M_2/M_1$, and luminosity ratio, $\mathcal{S} = F_2/F_1$, where F_i is the flux of the i th component:

$$\mathcal{A} = \frac{q}{(1+q)^{2/3}} \left(1 - \frac{\mathcal{S}(1+q)}{q(1+\mathcal{S})} \right). \quad (2)$$

For a nonluminous companion, $\mathcal{S} = 0$, and its mass can be extracted from Equation (2) using the measured AMRF value and the estimated M_1 .

Assuming the most stringent constraints on the mass and luminosity ratios for different companion types, Shahaf et al. (2023) defined the limiting AMRF values for an MS companion, \mathcal{A}_{MS} , or an MS+MS binary companion, \mathcal{A}_{TR} . Figure 1 shows

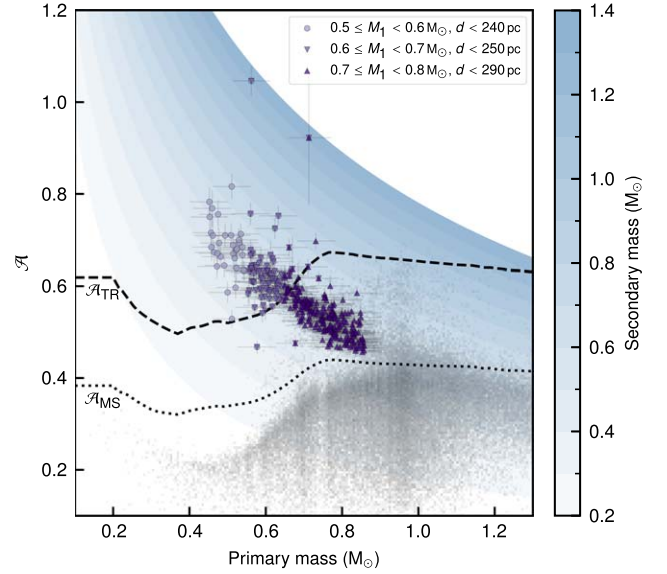


Figure 1. The Gaia DR3 AMRF (\mathcal{A}) as a function of the primary mass. The maximal possible AMRF values for an MS secondary (\mathcal{A}_{MS}) and an MS close binary (\mathcal{A}_{TR}) companion are marked by the dotted and dashed lines, respectively. The underlying light gray density plot shows the measured values from Gaia DR3 (after applying some quality cuts on the astrometric solutions; see Shahaf et al. 2023). Our selected volume-limited samples of high-probability MS+WD systems with different primary masses (see legend) are plotted with purple markers and gray error bars. Note that because of the primary mass uncertainty, there is some overlap between the samples. The expected AMRF values of WD companions of different masses are marked by blue shaded stripes, ranging from $0.2 M_\odot$ (light blue) to $1.4 M_\odot$ (dark blue) in steps of $0.1 M_\odot$.

the full distribution of the measured AMRF values from Gaia DR3 as a function of the primary mass (after applying some quality cuts on the astrometric solutions; see Section 3.1 of Shahaf et al. 2023). The maximal expected AMRF values assuming an MS+MS binary or a hierarchical MS+MS+MS triple system are marked by the dotted and dashed lines, respectively. These values separate the astrometric non-single-star sample into three classes: class I ($\mathcal{A} < \mathcal{A}_{\text{MS}}$), where the companion is most likely a single MS star; class II ($\mathcal{A}_{\text{MS}} < \mathcal{A} < \mathcal{A}_{\text{TR}}$), where the companion cannot be a single MS star but can still be a close binary of two MS stars; and class III ($\mathcal{A}_{\text{TR}} < \mathcal{A}$), where the companion is neither a single MS star nor a close MS binary but a likely compact object.

Based on Gaia DR3 data, Shahaf et al. (2023) compiled a sample of high-probability class III binary systems consisting of an MS and a compact object. Using Gaia synthetic photometry, calculated based on Gaia’s low-resolution BP/RP spectra, Shahaf et al. (2024) identified systems with a significant excess red color to further differentiate between class II hierarchical MS triple systems and binaries with a compact-object companion. While an MS companion(s) is expected to contribute flux in the redder wavelengths, the light contribution of a WD companion to the Gaia band is expected to be negligible (due to the extreme size ratio), unless it is very hot and young; then it contributes to the bluer end of the spectrum (see Shahaf et al. 2024 for details). This procedure resulted in a much more comprehensive catalog of nearly 3200 high-probability binary systems consisting of an MS and a compact object, most of them in the WD mass range. The orbital separations of these systems, on the order of 1 au, place them in a largely unexplored region of parameter space, with only a few such systems known previously (Anguiano et al.

2022; Parsons et al. 2023). In addition, these systems are not easily reproduced by standard binary population synthesis codes (see discussion in Shahaf et al. 2024).

Here we focus on a volume-complete sample of likely MS+WD binaries, following the method of Shahaf et al. (2024; see Section 2.2 below). We should note that this triage method relies on Gaia’s astrometric solutions (Halbwachs et al. 2023) along with the primary mass estimates reported by Gaia (Gaia Collaboration et al. 2023a). It is possible that despite the precautions taken by Shahaf et al. (2023, 2024), some spurious results still got through. However, for the mass ratios discussed in this paper and for MS primaries, the contamination by spurious detections is expected to be small. Spectroscopic follow-up observations of the subsample used here should verify the validity of the results.

2.2. Sample Selection

We start by selecting systems from the original catalog of Shahaf et al. (2023) that are unlikely to contain an MS companion,

$$\text{Pr(I)} < 10^{-3}, \quad (3)$$

where Pr(I) is the probability of being a class I system. This leaves 7687 out of 101,380 systems of the cleaned sample of Shahaf et al. (2023).

Following Shahaf et al. (2024), we select only systems satisfying

$$M_1 < 1.2 M_\odot + \Delta M_1, \quad (4)$$

where ΔM_1 is the uncertainty of the primary mass estimate. By this, we avoid systems with primaries that have already left the MS, rendering their mass estimate based on the location on the H-R diagram unreliable, leaving 6880 systems.

Next, we remove systems that are likely to be triple-MS systems by excluding 3846 probable class II systems with red excess flux (as mentioned above, WD companions are not expected to contribute any detectable flux in the redder wavelengths):

$$(\text{Pr(II)} \geq 0.5) \text{ and } (\text{Pr(red)} \geq 0.56), \quad (5)$$

where Pr(II) is the probability of being a class II system and Pr(red) is the probability of the presence of red excess flux compared to the predicted location of the photometric primary on the H-R diagram, assuming a total age of 2 Gyr and the estimated metallicity of each system (see Shahaf et al. 2024, for details). The red-excess probability was calculated using Gaia’s synthetic photometry in the Johnson–Kron–Cousins photometric system over the V versus $B-I$ plane. We further exclude an additional 145 class II systems that do not have color-excess data. This resulted in a total of 2889 systems that are likely to contain a WD companion.

To ensure a flux ratio of $\lesssim 10\%$ in the Gaia G band between the WD and the MS (see Figure 14 of Shahaf et al. 2024), keeping our dark-companion assumption justified, we focus only on systems with

$$M_1 \geq 0.5 M_\odot, \quad (6)$$

leaving 2835 systems. This assumption is crucial for the secondary mass estimates. On the high-mass end, we limit our

focus to systems with

$$M_1 < 0.8 M_\odot \quad (7)$$

in order to ensure a sensitivity to $\approx 0.6 M_\odot$ companions and to avoid the artificial excess of systems with $M_1 \approx 1 M_\odot$ resulting from the primary mass estimate process of Gaia Collaboration et al. (2023a; see underlying density plot in Figure 1 and discussion in Shahaf et al. 2024). This leaves a total of 1745 systems.

As discussed in Shahaf et al. (2024), this selection procedure based on red-excess probability minimizes the false-positive MS+WD identification rate at the expense of a higher false-negative rate (i.e., some true MS+WD systems are excluded from the sample). Systems with primary (MS) masses smaller than $\sim 0.6 M_\odot$ are more likely to have erroneous metallicity estimates, affecting the red-excess probability calculation (Shahaf et al. 2024). However, since the expected mass range of WD companions with M dwarf primaries resides within class III on the AMRF plot (see Figure 1), we overcome this misclassification here by applying the red-excess cut on class II systems only (Equation (5)). True MS+WD systems with primary (MS) masses higher than $\sim 0.6 M_\odot$ are more likely to be excluded due to erroneous primary mass estimates, especially those with masses around $\sim 1 M_\odot$ (Shahaf et al. 2024). Others can be missed if the primary has started to evolve off the MS (which would affect our red-excess estimation). As mentioned above, we avoid these problems by selecting systems with smaller primary masses.

The Gaia DR3 non-single-star catalog contains only sources satisfying (Halbwachs et al. 2023, Equation (16))

$$\frac{\varpi}{\sigma_\varpi} > \frac{20,000 \text{ days}}{P}, \quad (8)$$

where ϖ and σ_ϖ are the parallax and its error and P is the orbital period. Translating it using Kepler’s law to a constraint on the orbital separation, a , we get

$$\frac{a}{\text{au}} > 0.144 \left(\frac{M_1 + M_2}{M_\odot} \right)^{\frac{1}{3}} \left(\frac{\sigma_\varpi}{\text{mas}} \right)^{\frac{2}{3}} \left(\frac{d}{\text{pc}} \right)^{\frac{2}{3}}, \quad (9)$$

where d is the distance and $M_{1,2}$ are the component masses. For the median parallax error of our subsample (≈ 0.03 mas, with a typical relative error of about 4%), and for the limiting case of $M_1 = 0.8 M_\odot$ and $M_2 = 1.4 M_\odot$, we get

$$\frac{a}{\text{au}} > 0.018 \left(\frac{d}{\text{pc}} \right)^{\frac{2}{3}}, \quad (10)$$

or $a \gtrsim 0.79$ au at a distance of 290 pc (see below). We thus select only systems satisfying

$$a > 0.8 \text{ au}, \quad (11)$$

resulting in 1611 systems.

Next, we evaluate the completeness of our sample. Figure 2 shows the cumulative number of systems satisfying the above conditions as a function of the probed volume. To take into account the Lutz–Kelker bias (Lutz & Kelker 1973; Luri et al. 2018), causing the mean observed parallax to be systematically larger than its true value, the distance to each system is taken as the median value of $1/\varpi$ calculated based on 10,000 realizations of the parallax drawn from a Gaussian distribution defined using the observed Gaia parallax value and uncertainty.

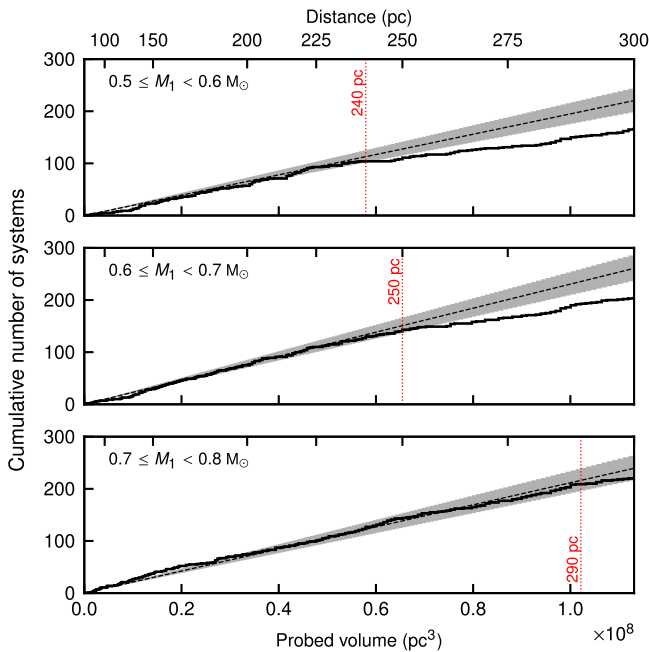


Figure 2. Cumulative number of systems as a function of the probed volume (solid line) for a variety of photometric primary mass bins (top: $0.5 M_{\odot} \leq M_1 < 0.6 M_{\odot}$; middle: $0.6 M_{\odot} \leq M_1 < 0.7 M_{\odot}$; bottom: $0.7 M_{\odot} \leq M_1 < 0.8 M_{\odot}$). The dashed line shows the expected number assuming a constant space density (calculated based on the total number of systems per sample at a maximal distance of 225 pc), and the gray region highlights its Poisson uncertainty. The dotted red line marks the selected maximal distance for each sample.

For a complete sample, we assume that the total number of systems grows linearly with the enclosed volume, i.e., a uniform number density. We estimate the number density based on the total number of systems within 225 pc and check at which distance the cumulative number of systems significantly deviates from the expected number of systems, assuming Poisson uncertainty. We do not fit the cumulative distribution directly, as its steps are not statistically independent (e.g., Hollands et al. 2018). We check the completeness of the sample for different photometric primary mass bins and find that the subsample of systems with photometric primaries with $0.5 M_{\odot} \leq M_1 < 0.6 M_{\odot}$ (within 1σ uncertainty) is more or less complete to a distance of ≈ 240 pc, the subsample of systems with photometric primaries of $0.6 M_{\odot} \leq M_1 < 0.7 M_{\odot}$ is complete within a distance of ≈ 250 pc, and the subsample of systems with $0.7 M_{\odot} \leq M_1 < 0.8 M_{\odot}$ is complete within a distance of ≈ 290 pc. We thus define three volume-complete subsamples:

- (i) $0.5 M_{\odot} \leq M_1 < 0.6 M_{\odot}$, $d < 240$ pc (116 systems);
- (ii) $0.6 M_{\odot} \leq M_1 < 0.7 M_{\odot}$, $d < 250$ pc (151 systems); and
- (iii) $0.7 M_{\odot} \leq M_1 < 0.8 M_{\odot}$, $d < 290$ pc (229 systems)

as our final samples (see Figure 1). We note that because of the primary mass uncertainty, there is some overlap between the samples. A total of 314 systems have passed these selection criteria and are listed in Table 1. The $0.5 M_{\odot} \leq M_1 < 0.6 M_{\odot}$ sample is the only one that probes the full WD mass range, where the expected AMRF values of systems with $\gtrsim 0.2 M_{\odot}$ companions are higher than the maximal AMRF value of an MS+MS binary. The other two samples are biased toward more massive WDs, as $\lesssim 0.6 M_{\odot}$ WD companions in this primary mass range are expected to be classified as class I systems (see Figure 1).

We also define a larger-yet-biased and volume-incomplete sample of systems with no red color excess, for reference. This sample is selected from the 6880 systems that have passed the selection criteria listed in Equations (3) and (4), with the additional no-red-color-excess condition,

$$\text{Pr}(\text{red}) \geq 0.56, \quad (12)$$

resulting in 2135 systems. Note that this condition applies to both class II and class III systems, unlike the one in Equation (5), to avoid the artificial excess of systems with $M_1 \approx 1 M_{\odot}$ (see above).

See Appendix A for the system properties of the different selected samples.

3. Results

Figure 3 shows the secondary mass distribution of our three volume-limited samples, as well as of our volume-incomplete no-red-color-excess sample. To take the mass uncertainty into account, we represent each star’s contribution to the distribution with a Gaussian mass probability distribution having the measured mean and standard deviation of the secondary mass. We then calculate the secondary mass distribution of our sample by summing all of the Gaussians into mass bins between 0 and $1.8 M_{\odot}$ in $0.025 M_{\odot}$ steps. We compare our results to the observed mass distributions of single WDs in the field. We calculate these distributions in a similar way (summing Gaussians) using the published catalogs of Kilic et al. (2020), Jiménez-Esteban et al. (2023), and O’Brien et al. (2024). Finally, we normalize each distribution by its maximal value, making the comparison between the height of the main $\approx 0.6 M_{\odot}$ peak and that of the high-mass bump insensitive to the inclusion of low-mass WDs.

The WD mass distribution of O’Brien et al. (2024) is based on the mass estimates of 1051 out of 1076 WDs in the volume-complete 40 pc WD sample.⁴ The WD masses in this catalog were estimated by fitting their spectral energy distributions (SEDs) using theoretical WD models after determining their spectral type spectroscopically. These masses were then corrected to account for inaccuracies in the low-mass models (O’Brien et al. 2024).

The samples of Kilic et al. (2020) and Jiménez-Esteban et al. (2023) are both based on the 100 pc WD sample. The WD mass distribution of Jiménez-Esteban et al. (2023) is based on 5728 hydrogen-dominated (DA) WDs hotter than 5500 K within 100 pc. The WD mass distribution of Kilic et al. (2020) is based on 1351 DA WDs hotter than 6000 K within 100 pc and the SDSS footprint, where their spectroscopically confirmed catalog is 83% complete. The WD masses in both catalogs were also estimated by fitting their SEDs using theoretical WD models after verifying spectroscopically that they have hydrogen-dominated atmospheres (using SDSS and follow-up spectra in Kilic et al. 2020 and Gaia’s low-resolution BP/RP spectra in Jiménez-Esteban et al. 2023).

Figure 4 shows the cumulative fraction of massive WDs relative to the full distribution of each sample (see Appendix B for the fitting procedure used to estimate the high-mass

⁴ For 25 WDs in this sample, the mass could not be determined reliably due to contamination from nearby stars or the presence of collision-induced absorption or strong molecular carbon absorption bands (O’Brien et al. 2024). For an additional $0.57 M_{\odot}$ WD (WD J181706.50+132824.99), we changed the mass uncertainty from the reported $0.00 M_{\odot}$ to $0.001 M_{\odot}$, the same as that of another WD (WD J074538.43–335551.34) with a similar log g error.

Table 1
The Selected Sample

Gaia DR3 ID	R.A. (deg)	Decl. (deg)	ϖ (mas)	M_1 (M_\odot)	M_2 (M_\odot)	P (days)	e
3598782754069068032	176.2898023	-5.7129768	4.801 ± 0.048	$0.452^{+0.049}_{-0.051}$	0.635 ± 0.043	862 ± 14	0.144 ± 0.027
5299929002634004480	136.5975904	-60.7005195	6.394 ± 0.042	$0.453^{+0.049}_{-0.051}$	0.594 ± 0.036	507.7 ± 1.4	0.397 ± 0.012
868863951177644160	115.5600885	25.9453065	5.72 ± 0.11	$0.456^{+0.051}_{-0.050}$	0.555 ± 0.043	465.2 ± 2.4	0.069 ± 0.024
2856698098507352064	3.4980152	26.9011924	4.217 ± 0.073	$0.458^{+0.050}_{-0.050}$	0.519 ± 0.036	593.5 ± 5.5	0.091 ± 0.045
4263071704959743360	288.9649287	-0.8243133	4.36 ± 0.10	$0.460^{+0.050}_{-0.051}$	0.627 ± 0.053	546.7 ± 4.9	0.060 ± 0.053
2566461354152574976	21.0477577	7.9769125	5.33 ± 0.11	$0.461^{+0.051}_{-0.050}$	0.553 ± 0.044	616.7 ± 3.5	0.051 ± 0.043
224549450109569536	54.6271642	39.2316386	7.576 ± 0.051	$0.465^{+0.050}_{-0.050}$	0.514 ± 0.030	484.24 ± 0.93	0.035 ± 0.011
6685604337007194368	300.3137539	-44.6334559	4.936 ± 0.037	$0.472^{+0.050}_{-0.050}$	0.486 ± 0.028	519.5 ± 2.3	0.064 ± 0.032
6218848456877200640	220.6254098	-29.3426568	4.62 ± 0.16	$0.473^{+0.051}_{-0.050}$	0.521 ± 0.048	810 ± 39	0.154 ± 0.080
159844874438662400	70.3915029	32.2002141	10.467 ± 0.044	$0.475^{+0.050}_{-0.050}$	0.630 ± 0.042	973 ± 25	0.080 ± 0.020

Note. ϖ is the parallax, M_1 is the mass of the MS component, M_2 is the mass of the WD, P is the orbital period, and e is the eccentricity. The full table is available in the supplemental information accompanying this publication.

(This table is available in its entirety in machine-readable form in the [online article](#).)

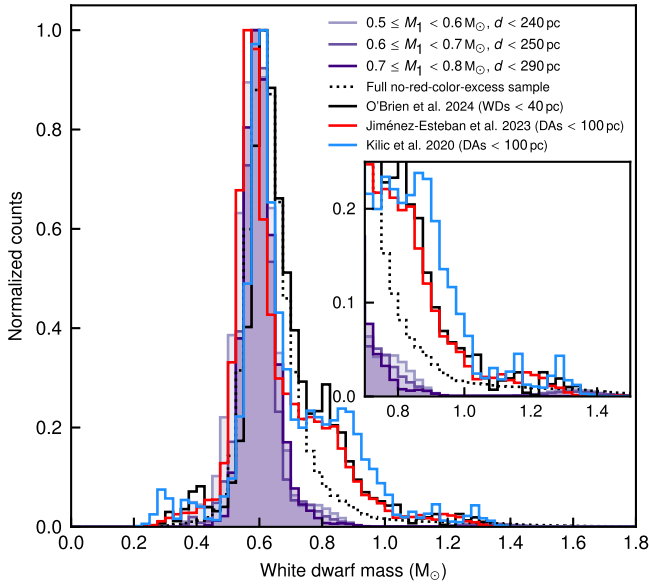


Figure 3. Secondary mass distribution of the selected volume-limited samples with MS primaries of $0.5 M_\odot \leq M_1 < 0.6 M_\odot$, $0.6 M_\odot \leq M_1 < 0.7 M_\odot$, and $0.7 M_\odot \leq M_1 < 0.8 M_\odot$ (purple shaded bars) and the full no-red-color-excess sample (dotted black). The observed distribution of the full 40 pc WD sample of O’Brien et al. (2024; solid black) and the magnitude-limited 100 pc hydrogen-dominated (DA) WD samples of Jiménez-Esteban et al. (2023; solid red) and Kilic et al. (2020; solid blue) are plotted for reference. The inset panel zooms in on the high-mass end of the distribution.

fraction). We find that while the high-mass bump constitutes a significant fraction of the 100 pc field WD sample— $40.6\% \pm 1.7\%$ in the sample of Kilic et al. (2020), $36.1\% \pm 0.8\%$ in that of Jiménez-Esteban et al. (2023), and $33.1\% \pm 1.6\%$ in that of O’Brien et al. (2024)—it contributes as much as $2.92\% \pm 0.02\%$ ($4.16\% \pm 0.04\%$) in our sample of WDs in astrometric binaries with $0.5 M_\odot \leq M_1 < 0.6 M_\odot$ ($0.6 M_\odot \leq M_1 < 0.7 M_\odot$).⁵ In other words, the fraction of WDs more massive than $\sim 0.7 M_\odot$ in binaries with K/M dwarf primaries and orbital separations of ~ 1 au is smaller by a factor of

⁵ No high-mass bump was detected for $0.7 M_\odot \leq M_1 < 0.8 M_\odot$; see Appendix B.

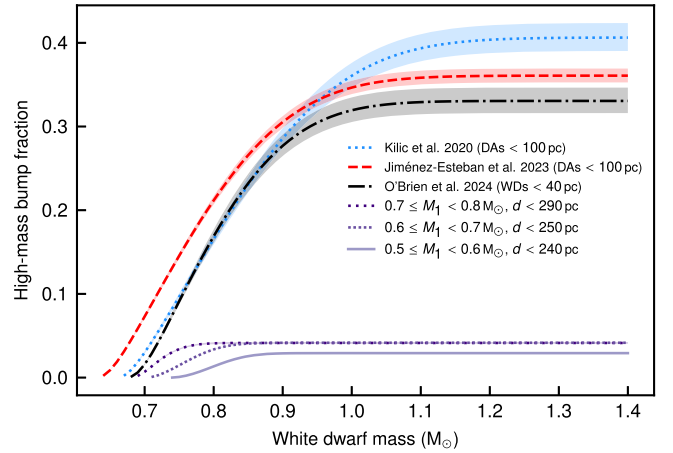


Figure 4. The cumulative fraction of massive WDs, relative to the full distribution. See Appendix B for the fitting procedure used to estimate the high-mass fraction.

~ 8 – 14 compared to their fraction among single WDs in the field.

4. Discussion

Figures 3 and 4 show a clear deficit of massive WDs in all of our MS+WD samples compared to the field WD samples. This is despite the bias against massive WDs in the magnitude-limited 100 pc field samples on the one hand (see Section 1) and Gaia’s higher observational sensitivity to astrometric binaries with more massive companions on the other hand. Such systems have higher AMRF values, which facilitate their detection and identification (see Figure 1). This deficit could arise from a selection effect, from an intrinsic physical difference between these two populations, or from a combination of the two.

4.1. Post-AGB-interaction Binaries

The orbital separation of ~ 1 au indicates that binary interaction of some kind was unavoidable when the WD was still in its red giant phase. At the same time, it rules out a common-envelope phase that should have brought the two stars much closer to each other. This suggests stable mass transfer as the interacting mechanism. The large eccentricities of some of

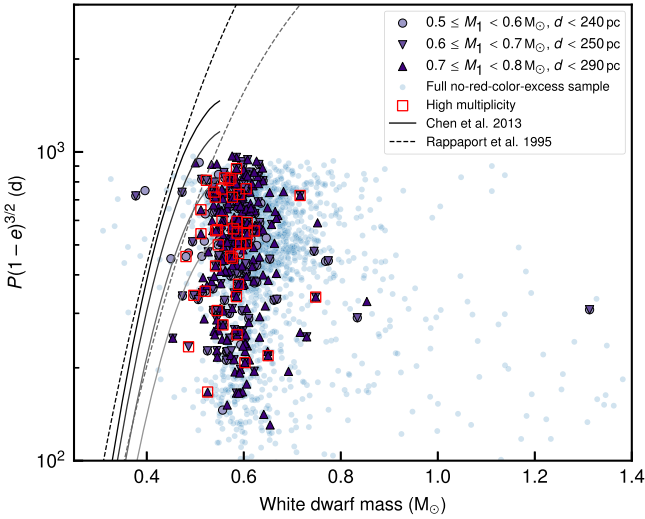


Figure 5. Mass–period relation of the selected samples (purple markers indicating different primary mass ranges as in Figure 1; see legend) and the full no-red-color-excess sample (blue dots). Systems of higher multiplicity (see Section 4.3) are marked by a red square. The solid lines show the theoretical relation from Chen et al. (2013) for different metallicities (from top to bottom, $Z = 0.02, 0.01, 0.004,$ and 0.001), while the dashed lines show the relation from Rappaport et al. (1995) for $Z = 0.02$ and 0.004 . The y-axis shows the orbital period, P , times $(1 - e)^{3/2}$, where e is the eccentricity (see Joss et al. 1987 for a derivation of this relation).

the systems in our sample (see Figure 8 in Appendix A) require an eccentricity pumping mechanism to counteract the circularization induced by the stable mass transfer (e.g., Van Winckel et al. 1995; Waelkens et al. 1996; Soker 2000; Bonačić Marinović et al. 2008; Izzard et al. 2010; Dermine et al. 2013; Vos et al. 2015; and see discussion in Shahaf et al. 2024).

Systems that have undergone stable mass transfer are expected to have some kind of a correlation between the mass of the WD and the orbital period (e.g., Joss et al. 1987; Rappaport et al. 1995; Chen et al. 2013). These relations have been calculated and tested for systems with low-mass WDs ($\lesssim 0.55 M_{\odot}$), i.e., when the WD progenitor was on the red giant branch (RGB). However, the relatively large masses of the majority of the WDs in our sample indicate that this stable mass transfer started when the WD progenitor was already on the asymptotic giant branch (AGB). Indeed, the mass–period relation of our observed sample is substantially different than that predicted for post-RGB interaction, with massive WDs in much shorter orbits than expected (Figure 5). Yet it is still likely that some kind of a mass–period relation does exist for post-AGB systems as well. Such a relation might impose an implicit prior on the WD mass distribution of our sample, given the preselected orbital separation range (determined by Gaia’s astrometric sensitivity).

The interaction on the AGB and the period–eccentricity relation of the systems in our sample resemble those of barium stars. Although a few known barium stars are found in the full MS +WD sample of Shahaf et al. (2024), none of them are part of the subsamples used here. This is not surprising, as known barium stars are usually more massive than the MS primaries included in our samples. Merle et al. (2016) have analyzed the s -process element abundance of a small sample of 11 WDs with measured masses orbiting cool (< 7000 K) stars. They showed that WDs less massive than $0.5 M_{\odot}$ do not have barium-star companions. This is expected, since the progenitors of $< 0.5 M_{\odot}$ WDs could not have reached the thermally pulsing AGB phase (Hurley et al. 2000). Kong et al. (2018) and Bharat Kumar et al. (2019) arrived at

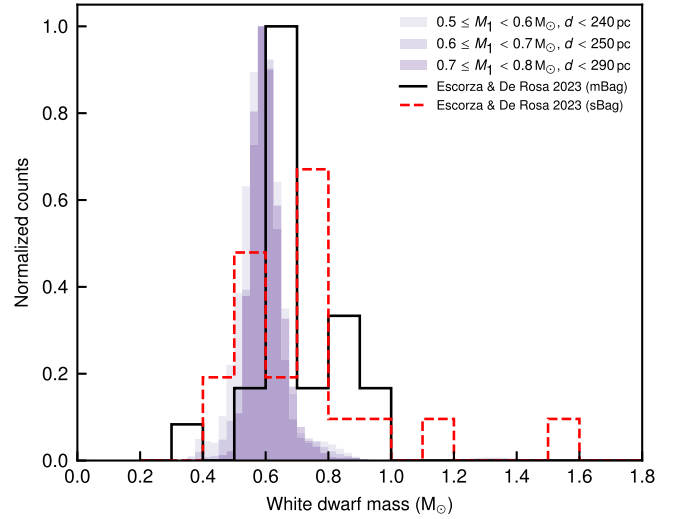


Figure 6. The WD mass distributions of our samples (purple shaded bars) compared to those of WDs orbiting mild barium giants (black solid line) and strong barium giants (red dashed line) from Escorza & De Rosa (2023).

similar conclusions based on a sample of 18 and 21 Sirius-like systems, respectively. For WDs with masses $> 0.51 M_{\odot}$, the results were inconclusive: some of the companions to massive WDs did not show evidence of s -process element enrichment, demonstrating that the mass of the WD progenitor is not the only parameter responsible for the creation of barium stars (with the other main suspects being the orbital separation and metallicity).

Recently, Escorza & De Rosa (2023) derived the mass distribution of WD companions to barium stars. They found a possible relation between the s -process element abundance in the barium red giant primary and the WD mass, where strongly polluted barium giants (“sBag”) tend to have more massive WD companions than mildly polluted barium giants (“mBag”). However, this relation was not sufficiently statistically significant (with a p -value of 0.45 in a Kolmogorov–Smirnov test). Figure 6 compares the mass distributions of the WD companions of strong and mild barium giants from Escorza & De Rosa (2023) and those of our volume-limited samples. Note that the samples of Escorza & De Rosa (2023) are not volume-complete, and their mass distributions presented in Figure 6 are regular histograms (normalized by the peak of the mild barium giant sample) and not the sum of Gaussians (see Section 3).

Figure 6 shows that the WD mass distributions of our samples peak at a slightly lower value than that of WDs orbiting mild and strong barium giants. A Kolmogorov–Smirnov test between our samples and the barium samples yielded p -values of $\lesssim 5 \times 10^{-9}$ for the mild barium giants and $\lesssim 10^{-4}$ for the strong barium giants, indicating a statistically significant difference between the samples. Assuming that the systems in our sample are post-AGB binaries, this might hint at a possible “continuum” of s -process element pollution, depending on the WD progenitor mass. In an ongoing follow-up program, we obtain mid-resolution spectra of systems in the AMRF sample (Shahaf et al. 2024). If this relation is correct, we expect to see a correlation between the s -process element abundance in the MS spectra and the mass of their WD companions (as suggested by Boffin & Jorissen 1988). Theoretical calculations by Karakas & Lugaro (2016) indicate that stars with initial masses of $\sim 2\text{--}4 M_{\odot}$ yield more s -process elements than lower- and higher-mass stars. In this case, the MS companions to the less-massive WDs in our

sample might lack any traces of *s*-process elements within the observational sensitivity. Since current post-AGB binary samples focus on barium stars, they can miss the lower- or higher-mass end of the underlying population. Gaia’s astrometric binary sample thus offers a more complete view of the population of post-AGB binaries.

If our samples indeed represent a population of post-stable-mass-transfer systems, then our primary mass selection implies an indirect prior on the initial mass ratio of the systems, since stable mass transfer is unlikely in cases of extreme mass ratios of the progenitor systems (Hjellming & Webbink 1987; Hurley et al. 2002). Thus, the deficit of massive WDs in our selected samples can be the result of the selection of the primary mass ($0.5\text{--}0.8 M_{\odot}$) and the orbital separation range probed by Gaia (which implies post-stable-mass-transfer binaries).

Yet when looking at our three different volume-limited samples, we see no significant difference between their resulting WD mass distributions (Figure 3), despite the different primary mass distributions. In other words, their present-day mass-ratio distribution is different (Figure 7 in Appendix A). Moreover, even when looking at the full no-red-color-excess sample, there is still a clear deficit of massive WDs compared to the field samples (see dotted black line in Figure 3). This sample contains MS primaries as massive as $\sim 1.2 M_{\odot}$ (Figure 7); thus, it does not exclude a priori systems with more massive WD companions. In addition, since this sample is not volume-limited, it is biased in favor of more massive MS primaries (due to their higher luminosities) and, as a consequence, of more massive WD companions. Furthermore, by excluding class I systems (Equation (3)), we exclude MS+WD systems with $\sim 0.6 M_{\odot}$ WDs and $\gtrsim 0.8 M_{\odot}$ MS primaries (see Figure 1). Since we normalize the WD mass distribution by the $\sim 0.6 M_{\odot}$ peak, the bias against $\sim 0.6 M_{\odot}$ WDs artificially increases the share of massive WDs in the normalized distribution. Yet despite these initial conditions biased in favor of massive WDs, there is still a lack of massive WDs in this no-red-color-excess sample compared to the field samples of WDs. Hence, the implicit prior on the initial mass ratio of the system does not seem to be the only reason for the massive-WD deficit.

4.2. Lack of Merger Products

There is growing evidence that a very large fraction of massive WDs are in fact merger products of binary evolution rather than descendants of single stars. There is a significantly smaller fraction of photospheric metal pollution from accretion of planetary debris in massive WDs compared to canonical-mass WDs (Koester et al. 2014). This could be explained by the complicated past of a merger-product WD, which makes it unlikely for planetary systems to survive the process. Other indications are the strong magnetic fields, rapid rotation rates, and high transverse velocities of many massive WDs (e.g., Kilic et al. 2023). The lack of massive WDs in the mass distribution of helium-dominated (DB) WDs (Bergeron et al. 2001; Gentile Fusillo et al. 2019; Tremblay et al. 2019) also agrees with the merger origin of massive WDs, as only rare mergers of DB+DB binaries will produce a massive DB WD. Maoz et al. (2018) have estimated the double-WD merger rate based on a large spectroscopic sample of WDs. They found that the merger rate is 4.5–7 times higher than the specific Type Ia supernova rate in the Milky Way, implying that a large fraction of present-day WDs should be merger products. Based on transverse velocities from Gaia,

Cheng et al. (2020) have estimated that about 20% of massive ($\gtrsim 0.8 M_{\odot}$) WDs have dynamical ages that are inconsistent with their cooling ages, indicating a merger origin. Fleury et al. (2022) have estimated that $\approx 40\text{--}50\%$ of WDs with masses of $1.15\text{--}1.25 M_{\odot}$ come from mergers by comparing their cooling age distribution with the star formation history. Theoretical binary population synthesis studies have also estimated a significant contribution of mergers to the currently single WD population of about 10%–30% (Toonen et al. 2017) or 9%–16% (Torres et al. 2022) of all single WDs and 30%–50% of the massive WDs (Temmink et al. 2020). Interestingly, there might be a hint of an additional small peak around $\approx 1.2 M_{\odot}$ in the mass distribution of field WDs, as can be seen in Figure 3. If this excess of $\approx 1.2 M_{\odot}$ WDs is indeed genuine, it might be the result of equal-mass double-WD mergers (of two $\approx 0.6 M_{\odot}$ WDs). This would be consistent with the “twin” peak discovered by El-Badry et al. (2019) in wide MS binaries from Gaia, and previous estimates of a higher fraction of merger products in this mass range (Cheng et al. 2020; Fleury et al. 2022).

Given the relatively small orbital separations (~ 1 au) of the MS+WD binaries in our sample, it is unlikely that a large number of the WD companions in these systems (if any) are merger products of an inner binary in a previously hierarchical triple system, since the hypothetical inner binary could not have had enough room to evolve and merge. In the most extreme case, where the difference between our samples and field samples stems only from the lack of merger products, it implies that almost all WDs more massive than $\sim 0.7 M_{\odot}$ come from mergers. However, since we have no accurate knowledge of the initial mass-ratio distribution of our sample and of the stable mass-transfer mechanism these systems have undergone, we cannot confidently quantify the contribution of mergers compared to the field samples.

4.3. Searching for Tertiary Companions

Recently, Shariat et al. (2023) suggested that at least 30% of solar-type stars in the local neighborhood were born in hierarchical triples, based on simulations and on the Gaia 200 pc sample. From their simulations, Shariat et al. (2023) find that the inner binaries in the majority of these triples merge and that only a few percent remain in an MS+WD configuration within the Galaxy lifetime. Since the orbital separations of the inner binaries in those systems are typically on the order of ~ 1 au as well, we have searched the Gaia DR3 catalog for tertiary companions within a projected separation of 1 pc around the MS+WD binaries in our selected subsamples. See Appendix C for the details of this search. We find tertiary companions to 44 out of our 314 systems ($\approx 14\%$), as listed in Table 2, in consistency with Shariat et al. (2023). This is also consistent with the lack of merger products assumption (see Section 4.2), since the systems with merged inner binaries have much larger orbital separations.

The eccentricities of the inner binaries in these systems are not different than those of the nontriple systems in our sample (Figure 8) and are somewhat lower than those of the simulated systems of Shariat et al. (2023, C. Shariat, private communication). The tertiary companions are almost always less massive than the primary MS in the inner binary (see Figure 10). This might be a selection effect, since in systems with more massive tertiaries, the tertiary is more likely to have evolved into a compact object, making it harder to detect. A few of these systems might actually be quadruple systems,

composed of an inner MS+WD binary and an outer MS+WD binary companion, based on their location on the H-R diagram between the MS and the WD sequence (see Figure 11). Triple systems in which the tertiary is an evolved star—especially a single WD—are of particular interest, since the tertiary can be used to estimate the total age of the system and thus constrain the binary evolution and initial-to-final mass relation of the WD in the inner binary. In our subsample, there are three such systems with WD tertiaries. However, in two of them, the tertiary seems to be an extremely low-mass WD that could not have evolved from a single star in the Universe's lifetime. We defer the analysis of these systems and an expanded search for tertiary companions in the full MS+WD catalog of Shahaf et al. (2024) to an upcoming publication.

5. Summary and Conclusions

In this study, we find a stark deficit of massive WD companions in volume-complete samples of binaries with K/M dwarf primaries and orbital separations of ~ 1 au compared to their occurrence among single WDs in the field. These systems are likely to have undergone a phase of stable mass transfer when the WD progenitor was on the AGB. This might indicate an implicit mass-ratio and/or WD mass prior selection explaining (part of) this deficit. In addition, given the relatively small orbital separations, these systems are unlikely to contain WDs that are merger products.

These subsamples, as well as the full sample from which they were drawn (Shahaf et al. 2023, 2024), provide a unique opportunity to study the population of post-AGB-interaction binaries (barium stars included), which is currently poorly constrained by observations. The discovery of stable mass-transfer WD+M dwarf binaries with orbital periods of a few hundred days contradicts previous assumptions on the possible existence of such systems (Lagos et al. 2022). In addition, it adds to the accumulating evidence that a large fraction of the massive WDs in the field are merger products. This has implications for many astrophysical and cosmological questions. The merger rate and mass distribution of WDs directly affect the expected rate of Type Ia supernovae (assuming double-degenerate scenarios; e.g., Maoz et al. 2018) and the expected gravitational-wave foreground and detectable sources for the Laser Interferometer Space Antenna (Korol et al. 2022). It also affects the expected occurrence rate of massive-WD companions in short-period binaries with compact companions (e.g., Mazeh et al. 2022).

Acknowledgments

We thank Boris Gänsicke and Dan Maoz for pointing out that the narrow distribution and lack of a high-mass tail in the mass distribution of DB WDs hints at a merger origin, Cheyenne Shariat for suggesting that some of the systems might have tertiary companions, and the anonymous referee for valuable comments.

The research of S.S. is supported by a Benziyo prize postdoctoral fellowship. S.B.A. and T.M. acknowledge support from the Israel Ministry of Science grant IMOS 714193-02. S. B.A.'s research is supported by the Peter and Patricia Gruber Award, the Azrieli Foundation, the André Deloro Institute for Advanced Research in Space and Optics, the Willner Family Leadership Institute for the Weizmann Institute of Science, and the Israel Science Foundation grant ISF 714022-02. S.B.A. is the incumbent of the Aryeh and Ido Dissentshik Career Development Chair.

This work has made use of data from the European Space Agency (ESA) mission Gaia (<https://www.cosmos.esa.int/gaia>), processed by the Gaia Data Processing and Analysis Consortium (DPAC; <https://www.cosmos.esa.int/web/gaia/dpac/consortium>). Funding for the DPAC has been provided by national institutions, in particular the institutions participating in the Gaia Multilateral Agreement.

Facility: Gaia.

Software: astropy (Astropy Collaboration et al. 2013, 2018), matplotlib (Hunter 2007), numpy (Oliphant 2006; van der Walt et al. 2011), scipy (Virtanen et al. 2020), topcat (Taylor 2005).

Appendix A Sample Properties

Figure 7 shows the parallax error, inclination, transverse velocity, projected semimajor axis, period, eccentricity, metallicity, primary mass, and mass-ratio distributions of our volume-limited samples, along with the full no-red-excess sample, for reference. No significant difference is seen between these samples. The estimated metallicities of systems with $\lesssim 0.6 M_{\odot}$ primaries are generally unreliable (see Shahaf et al. 2024), explaining the different metallicity distributions of the $0.5 M_{\odot} \leq M_1 < 0.7 M_{\odot}$ subsamples. The eccentricity as a function of the orbital period is shown in Figure 8 (see discussion in Section 4). Table 1 includes the full selected sample (all 314 systems that have passed the selection criteria listed in Section 2.2).

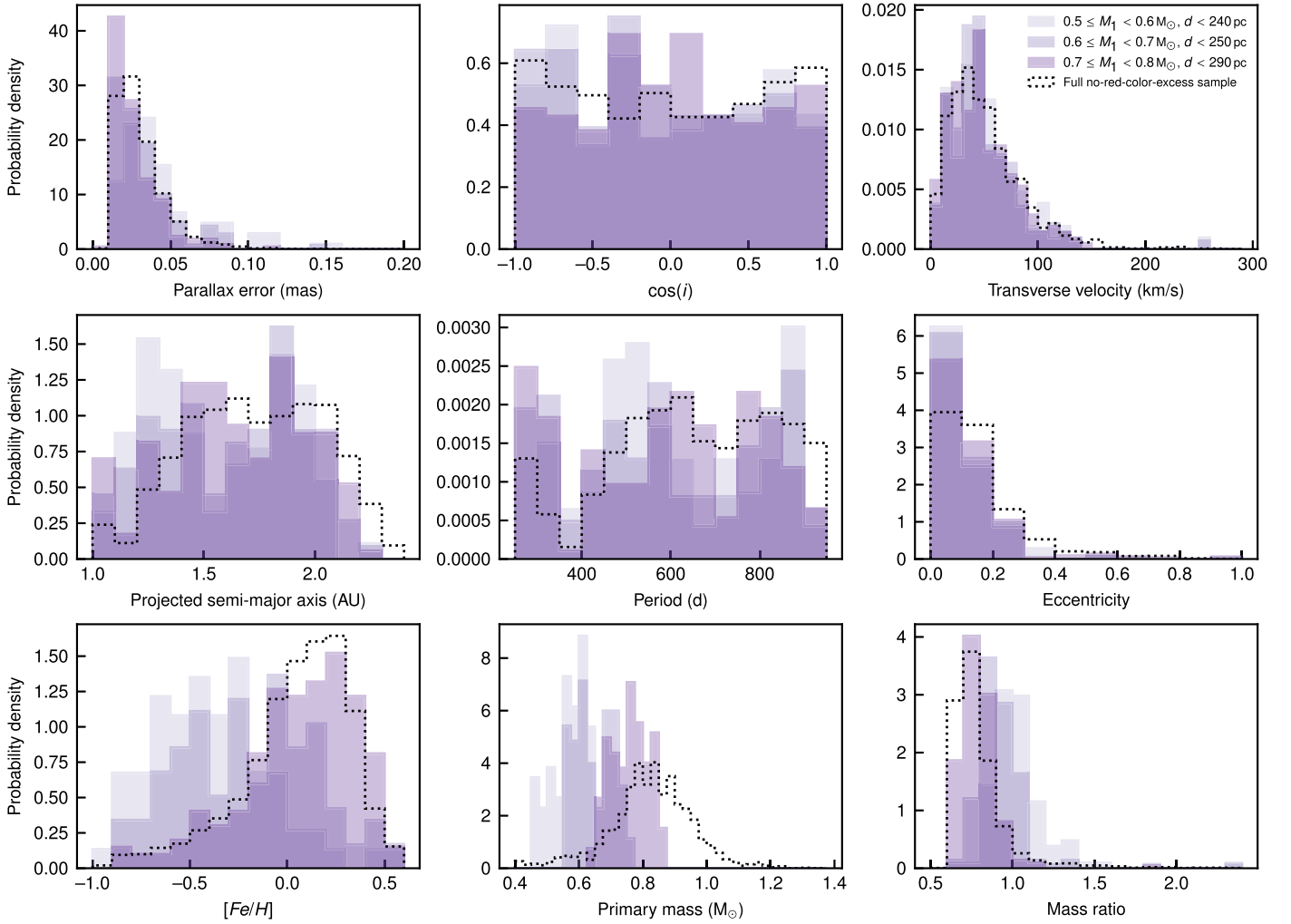


Figure 7. Histograms of the parallax error, cosine of the inclination angle, transverse velocity, projected semimajor axis, period, eccentricity, metallicity, primary mass, and mass ratio (from right to left, top to bottom) of the selected volume-limited samples and the reference full no-red-color-excess sample. The dips in the period around 1 and 2 yr are a result of Gaia’s mission duration.

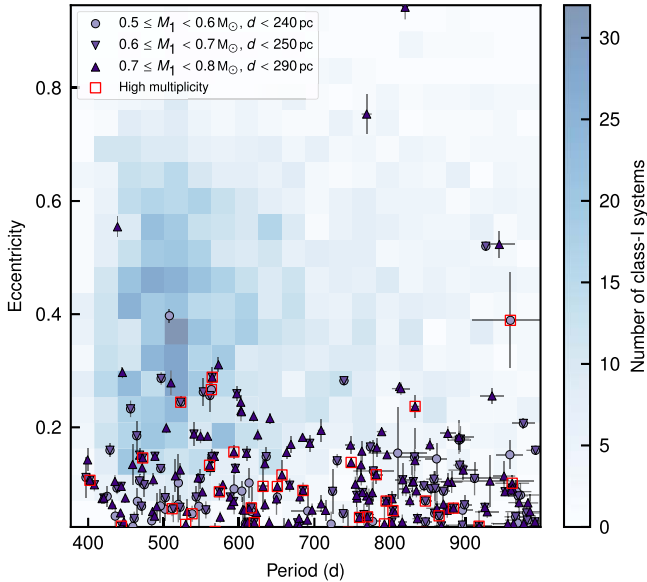


Figure 8. Period–eccentricity relation of the selected samples (purple markers with black error bars). Systems of higher multiplicity (see Section 4.3) are marked by a red square. The two-dimensional histogram of a class I ($\text{PrI} > 0.9$) subsample with the same constraints on the primary mass, orbital separation, and distance is plotted in blue shades for reference.

Appendix B Estimating the High-mass Fraction

In order to compare the different distributions, we fit each sample with a combination of two Gaussians, $\mathcal{G}(\mu_1, \sigma_1) + n\mathcal{G}(\mu_2, \sigma_2)$, normalized by the maximal peak, where

$$\mathcal{G}(\mu, \sigma) = \frac{1}{\sigma\sqrt{2\pi}} e^{-\frac{(x-\mu)^2}{2\sigma^2}} \quad (\text{B1})$$

is a Gaussian with mean μ and standard deviation σ and n is a constant. We fit the distribution using SCIPY’s CURVE_FIT trust region reflective algorithm, setting the initial positions of the Gaussians’ means to 0.6 and $0.8 M_\odot$ and the lower bound of the second Gaussian mean to $0.69 M_\odot$. Figure 9 shows the fit results for each of the samples. Note that no actual secondary peak is detected for the $0.7 M_\odot \leq M_1 < 0.8 M_\odot$ sample, and the secondary Gaussian’s mean is assigned the lower limiting value allowed for the fit. We thus exclude the Gaussian fit of this sample from the discussion.

We define the area enclosed between the two Gaussians, integrated from their intersection point and normalized by the area enclosed by the full double-Gaussian distribution, as the fraction of massive WDs in each sample. Figure 4 shows the

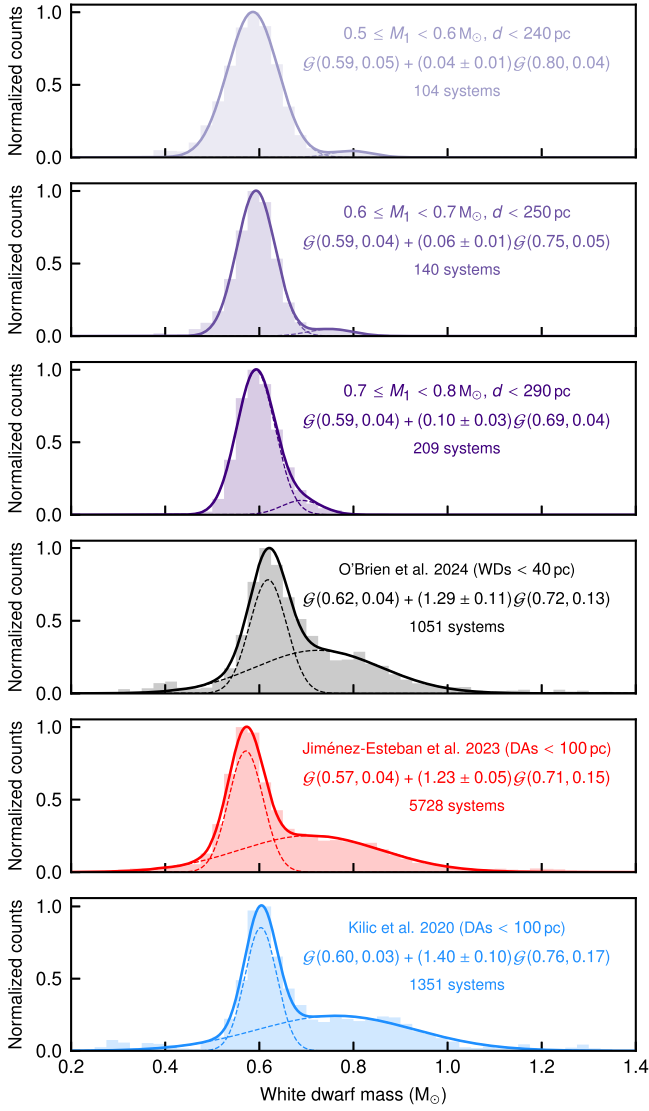


Figure 9. Double-Gaussian fit to the mass distribution of our final samples (top three panels), the 40 pc field sample of O’Brien et al. (2024; fourth panel), and the 100 pc field samples of Jiménez-Esteban et al. (2023; fifth panel) and Kilic et al. (2020; bottom panel). The bar plot shows the underlying observed distribution. The solid line shows the fitted function, while the dashed lines show the individual Gaussian components of the fit.

cumulative fraction of massive WDs. The shaded area in Figure 4 marks the uncertainty based on the 1σ error of the n coefficient (see Figure 9).

Appendix C Tertiary Search

We searched the single-star catalog of Gaia DR3 (`gaiadr3.gaiia_source`) for tertiary companions within a projected separation of 1 pc. We followed El-Badry et al. (2021), selecting sources with valid parallaxes (larger than 1 mas, with a signal-to-noise ratio larger than 5 and error smaller than 2 mas) and non-null G -band photometry. We further selected only sources with consistent parallaxes and proper motions (Equations (1)–(7) in El-Badry et al. 2021). We

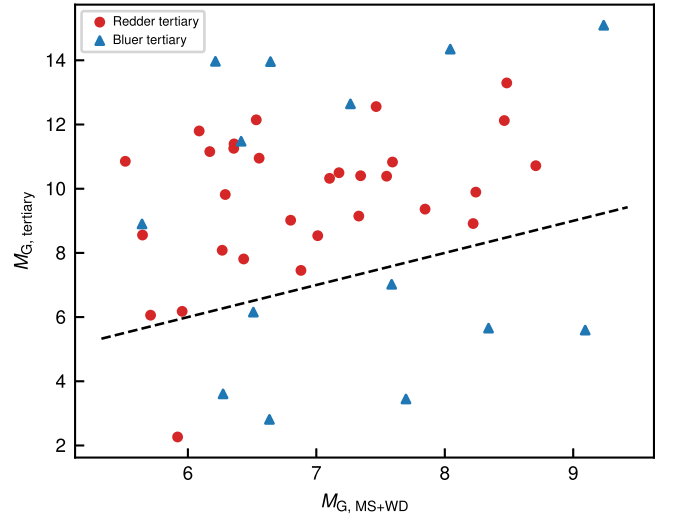


Figure 10. Dereddened absolute Gaia G -band magnitude of the tertiary companions vs. that of the corresponding inner binary. Systems where the tertiary has a redder (bluer) $G_{BP}-G_{RP}$ color are marked by red circles (blue triangles). The dashed black line corresponds to equal absolute magnitudes.

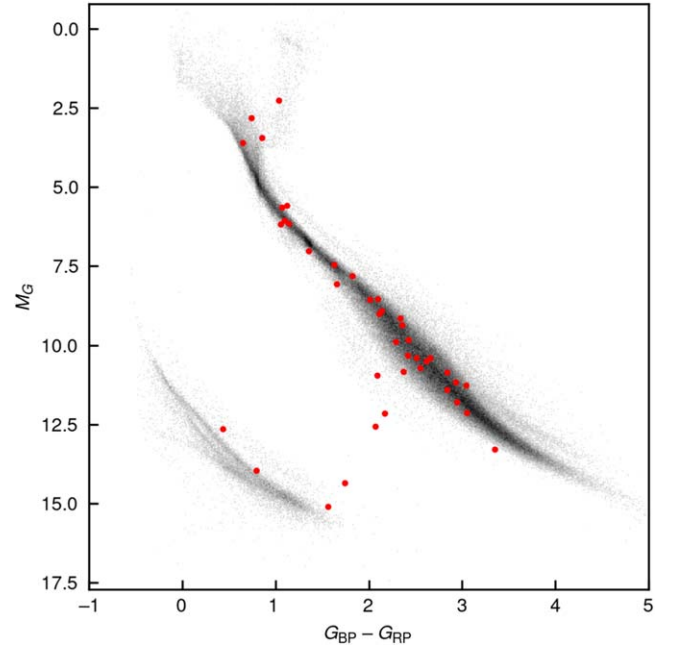


Figure 11. Gaia dereddened color–magnitude diagram for the tertiary companions in the higher-multiplicity systems in our sample (marked by red circles). The number density of the Gaia 100 pc sample is shown in gray scale for reference.

find 44 systems with tertiary companions. The results are listed in Table 2. Figure 10 compares the absolute magnitudes and colors of the tertiaries and their corresponding inner binaries. In most cases, the tertiaries are fainter and redder than the inner binaries, indicating a lower mass compared with the primary MS stars. Figure 11 shows the location of these tertiaries on the Gaia color–magnitude diagram.

Table 2
The High-multiplicity Systems in Our Sample

Gaia DR3 ID ₁	Gaia DR3 ID ₂	R.A. (deg)	Decl. (deg)	a_{out} (au)
41954481793705984	41947163169437312	51.3936258	14.1095859	$(6.449 \pm 0.067) \times 10^4$
613025599896017152	613025595603558656	146.2528781	11.6631120	$(2.7 \pm 1.4) \times 10^2$
811943986554770944	811943986554770304	140.0323833	38.4901015	7793 ± 67
1464711807899087872	1464710948905628544	195.7554838	30.7102862	4063 ± 25
1483641103161355520	1483641103161355648	211.5761748	37.6017495	1812 ± 41
1492136445393915008	1492136445393253760	214.9042418	41.5628127	$(2.25 \pm 0.45) \times 10^3$
1538567721922127872	1538567721921601024	185.1857278	43.9048691	$(5.3 \pm 1.6) \times 10^2$
1674635034638596608	1674635034638596480	206.7410714	70.1170684	4016 ± 63
1860726205116568960	1857719113838086528	309.2080331	29.6135867	$(1.0958 \pm 0.0036) \times 10^5$
1923185170017264768	1923185170014670720	352.3316075	39.7634623	$(1.43 \pm 0.40) \times 10^3$
1966726242802331008	1966726238496845184	324.2892688	41.8937876	$(3.94 \pm 0.16) \times 10^3$
2009304139089565824	2009304143391973120	349.6644490	57.2390633	473 ± 45
2038294210577929216	2038293798261077120	288.9527488	29.0814771	$12,559 \pm 39$
2151393206408068224	2151394683876818560	275.0641460	57.3197284	1435 ± 54
2200473069016427392	2200473069009862912	337.4862905	59.5666542	788 ± 73
2343910098928012928	2343910098928013056	10.7852972	-25.7370659	902 ± 30
2605394231962904064	2605395090956499968	346.2535778	-11.3645117	$(1.426 \pm 0.011) \times 10^4$
2673760597963293824	2673760593670425344	327.0004357	-2.5428920	$(7.7 \pm 1.2) \times 10^2$
2682585347007232640	2682585342712253440	333.0021960	2.0869376	4495 ± 84
3197547046716036480	3197547145498930432	61.8850833	-5.0470784	$(4.72 \pm 0.32) \times 10^3$
3363639445008582272	3363639440711596416	109.7579607	19.7387912	$(4.33 \pm 0.20) \times 10^3$
3466095099578873600	3466095099578872960	181.6494833	-33.8798655	1888 ± 42
4037114609474235264	4037114570697892224	270.8505810	-37.1188976	5445 ± 49
4069921356289901312	4069921356279221120	270.4503637	-22.1154815	$(2.39 \pm 0.16) \times 10^3$
4401090925658852352	4401090547701727616	234.3723657	-4.2793397	$14,516 \pm 56$
4465538043807424384	4465538043805350656	247.8194402	15.6409156	$(9.6 \pm 1.6) \times 10^2$
4640209037975567744	4640209037975567488	36.3436481	-75.3109028	2225 ± 46
4810205969559395584	4810205973855745920	75.1466966	-46.6567928	1651 ± 21
4983401560858949248	4983401560858949120	19.3615182	-43.7020454	424 ± 13
5015634534500904960	5015634530204196608	23.0808196	-32.9924135	$(3.33 \pm 0.10) \times 10^3$
5092889726161772416	5092890104118894080	63.0466602	-19.1807261	4811 ± 42
5491104349224057984	5491104353520148608	105.5992774	-55.1508980	2743 ± 25
5608254942340292352	5608254946640301696	103.3887846	-30.4734182	2518 ± 32
5790161689395101696	5790161689388304896	212.9604669	-75.4187154	7275 ± 23
5874328960960829312	5874328956628761216	222.1666976	-62.6258238	1143 ± 81
5882977513221448704	5882977513221446272	232.5871052	-57.8725815	2492 ± 21
5938730445019006592	5938762129005006720	256.7395782	-48.0432136	$(1.903 \pm 0.011) \times 10^5$
5979878155858301440	5979877679168231296	257.9089066	-32.8234753	$(4.015 \pm 0.069) \times 10^4$
6385252016957373824	6385252016957373952	338.6680990	-68.9519637	8619 ± 26
6396056127449928832	6396056127449928704	328.7035022	-69.2339582	4281 ± 43
6542671158289237248	6542671153994956800	345.1808744	-42.4306665	773 ± 59
6593522402843124992	6593522368483386240	338.1420104	-39.9830140	6493 ± 91
6784523000111321216	6784523000111320960	319.7664536	-30.8980630	1522 ± 75
6789344324239269760	6789343907626004608	321.2985621	-28.9285655	$(7.25 \pm 0.16) \times 10^4$

Note. The first ID is of the MS+WD inner binary, while the second ID and the coordinates are of the outer companion. a_{out} is the projected orbital separation of the outer companion.

ORCID iDs

Na'ama Hallakoun  <https://orcid.org/0000-0002-0430-7793>

Sahar Shahaf  <https://orcid.org/0000-0001-9298-8068>

Tsevi Mazeh  <https://orcid.org/0000-0002-3569-3391>

Silvia Toonen  <https://orcid.org/0000-0002-2998-7940>

Sagi Ben-Ami  <https://orcid.org/0000-0001-6760-3074>

References

Althaus, L. G., Córscico, A. H., Isern, J., & García-Berro, E. 2010, *A&ARv*, **18**, 471

Anguiano, B., Majewski, S. R., Stassun, K. G., et al. 2022, *AJ*, **164**, 126

Astropy Collaboration, Price-Whelan, A. M., Sipőcz, B. M., et al. 2018, *AJ*, **156**, 123

Astropy Collaboration, Robitaille, T. P., Tollerud, E. J., et al. 2013, *A&A*, **558**, A33

Bergeron, P., Dufour, P., Fontaine, G., et al. 2019, *ApJ*, **876**, 67

Bergeron, P., Leggett, S. K., & Ruiz, M. T. 2001, *ApJS*, **133**, 413

Bharat Kumar, Y., Kong, X. M., Zhao, G., & Zhao, J. K. 2019, in IAU Symp. 343, s-process abundances of Primary stars in the Sirius-like Systems: Constraints on pollution from AGB stars (Cambridge: Cambridge Univ. Press), 351

Boffin, H. M. J., & Jorissen, A. 1988, *A&A*, **205**, 155

Bonačić Marinović, A. A., Glebbeek, E., & Pols, O. R. 2008, *A&A*, **480**, 797

Caron, A., Bergeron, P., Blouin, S., & Leggett, S. K. 2023, *MNRAS*, **519**, A529

Chen, X., Han, Z., Deca, J., & Podsiadlowski, P. 2013, *MNRAS*, **434**, 186

Cheng, S., Cummings, J. D., Ménard, B., & Toonen, S. 2020, *ApJ*, **891**, 160

Córscico, A. H., De Gerónimo, F. C., Camisassa, M. E., & Althaus, L. G. 2019, *A&A*, **632**, A119

- Dermine, T., Izzard, R. G., Jorissen, A., & Van Winckel, H. 2013, *A&A*, **551**, A50
- El-Badry, K., Rix, H.-W., & Heintz, T. M. 2021, *MNRAS*, **506**, 2269
- El-Badry, K., Rix, H.-W., Tian, H., Duchêne, G., & Moe, M. 2019, *MNRAS*, **489**, 5822
- Escorza, A., & De Rosa, R. J. 2023, *A&A*, **671**, A97
- Falcon, R. E., Winget, D. E., Montgomery, M. H., & Williams, K. A. 2010, *ApJ*, **712**, 585
- Falcon, R. E., Winget, D. E., Montgomery, M. H., & Williams, K. A. 2012, *ApJ*, **757**, 116
- Fleury, L., Caiazzo, I., & Heyl, J. 2022, *MNRAS*, **511**, 5984
- Fontaine, G., Brassard, P., & Bergeron, P. 2001, *PASP*, **113**, 409
- Gaia Collaboration, Arenou, F., Babusiaux, C., et al. 2023a, *A&A*, **674**, A34
- Gaia Collaboration, Brown, A. G. A., Vallenari, A., et al. 2018, *A&A*, **616**, A1
- Gaia Collaboration, Brown, A. G. A., Vallenari, A., et al. 2021, *A&A*, **649**, A1
- Gaia Collaboration, Prusti, T., de Bruijne, J. H. J., et al. 2016, *A&A*, **595**, A1
- Gaia Collaboration, Vallenari, A., Brown, A. G. A., et al. 2023b, *A&A*, **674**, A1
- García-Berro, E., Kilic, M., & Kepler, S. O. 2016, *IJMPD*, **25**, 1630005
- Gatewood, G. D., & Gatewood, C. V. 1978, *ApJ*, **225**, 191
- Gentile Fusillo, N. P., Tremblay, P.-E., Gänsicke, B. T., et al. 2019, *MNRAS*, **482**, 4570
- Gentile Fusillo, N. P., Tremblay, P. E., Cukanovaite, E., et al. 2021, *MNRAS*, **508**, 3877
- Green, R. F., Schmidt, M., & Liebert, J. 1986, *ApJS*, **61**, 305
- Halbwachs, J.-L., Pourbaix, D., Arenou, F., et al. 2023, *A&A*, **674**, A9
- Hjellming, M. S., & Webbink, R. F. 1987, *ApJ*, **318**, 794
- Hollands, M. A., Tremblay, P. E., Gänsicke, B. T., Gentile-Fusillo, N. P., & Toonen, S. 2018, *MNRAS*, **480**, 3942
- Hunter, J. D. 2007, *CSE*, **9**, 90
- Hurley, J. R., Pols, O. R., & Tout, C. A. 2000, *MNRAS*, **315**, 543
- Hurley, J. R., Tout, C. A., & Pols, O. R. 2002, *MNRAS*, **329**, 897
- Izzard, R. G., Dermine, T., & Church, R. P. 2010, *A&A*, **523**, A10
- Jiménez-Esteban, F. M., Torres, S., Rebassa-Mansergas, A., et al. 2018, *MNRAS*, **480**, 4505
- Jiménez-Esteban, F. M., Torres, S., Rebassa-Mansergas, A., et al. 2023, *MNRAS*, **518**, 5106
- Joss, P. C., Rappaport, S., & Lewis, W. 1987, *ApJ*, **319**, 180
- Karakas, A. I., & Lugaro, M. 2016, *ApJ*, **825**, 26
- Kepler, S. O., Koester, D., Pelisoli, I., Romero, A. D., & Ourique, G. 2021, *MNRAS*, **507**, 4646
- Kepler, S. O., Pelisoli, I., Koester, D., et al. 2015, *MNRAS*, **446**, 4078
- Kepler, S. O., Pelisoli, I., Koester, D., et al. 2016, *MNRAS*, **455**, 3413
- Kepler, S. O., Pelisoli, I., Koester, D., et al. 2019, *MNRAS*, **486**, 2169
- Kilic, M., Bergeron, P., Kosakowski, A., et al. 2020, *ApJ*, **898**, 84
- Kilic, M., Moss, A. G., Kosakowski, A., et al. 2023, *MNRAS*, **518**, 2341
- Koester, D., Gänsicke, B. T., & Farihi, J. 2014, *A&A*, **566**, A34
- Kong, X. M., Zhao, G., Zhao, J. K., et al. 2018, *MNRAS*, **476**, 724
- Korol, V., Hallakoun, N., Toonen, S., & Karnesis, N. 2022, *MNRAS*, **511**, 5936
- Lagos, F., Schreiber, M. R., Parsons, S. G., et al. 2022, *MNRAS*, **512**, 2625
- Luri, X., Brown, A. G. A., Sarro, L. M., et al. 2018, *A&A*, **616**, A9
- Lutz, T. E., & Kelker, D. H. 1973, *PASP*, **85**, 573
- Maoz, D., Hallakoun, N., & Badenes, C. 2018, *MNRAS*, **476**, 2584
- Mazeh, T., Faigler, S., Bashi, D., et al. 2022, *MNRAS*, **517**, 4005
- McCleery, J., Tremblay, P.-E., Gentile Fusillo, N. P., et al. 2020, *MNRAS*, **499**, 1890
- Merle, T., Jorissen, A., Van Eck, S., Masseron, T., & Van Winckel, H. 2016, *A&A*, **586**, A151
- O'Brien, M. W., Tremblay, P. E., Gentile Fusillo, N. P., et al. 2023, *MNRAS*, **518**, 3055
- O'Brien, M. W., Tremblay, P. E., Klein, B. L., et al. 2024, *MNRAS*, **527**, 8687
- Oliphant, T. 2006, NumPy: A guide to NumPy (USA: Trelgol Publishing)
- Parsons, S. G., Hernandez, M. S., Toloza, O., et al. 2023, *MNRAS*, **518**, 4579
- Rappaport, S., Podsiadlowski, P., Joss, P. C., Di Stefano, R., & Han, Z. 1995, *MNRAS*, **273**, 731
- Rebassa-Mansergas, A., Rybicka, M., Liu, X. W., Han, Z., & García-Berro, E. 2015, *MNRAS*, **452**, 1637
- Shahaf, S., Bashi, D., Mazeh, T., et al. 2023, *MNRAS*, **518**, 2991
- Shahaf, S., Hallakoun, N., Mazeh, T., et al. 2024, *MNRAS*, **529**, 3729
- Shahaf, S., Mazeh, T., Faigler, S., & Holl, B. 2019, *MNRAS*, **487**, 5610
- Shariat, C., Naoz, S., Hansen, B. M. S., et al. 2023, *ApJL*, **955**, L14
- Soker, N. 2000, *A&A*, **357**, 557
- Taylor, M. B. 2005, in ASP Conf. Ser. 347, Astronomical Data Analysis Software and Systems XIV, ed. P. Shopbell, M. Britton, & R. Ebert (San Francisco, CA: ASP), 29
- Temmink, K. D., Toonen, S., Zapartas, E., Justham, S., & Gänsicke, B. T. 2020, *A&A*, **636**, A31
- Toonen, S., Hollands, M., Gänsicke, B. T., & Boekholt, T. 2017, *A&A*, **602**, A16
- Torres, S., Canals, P., Jiménez-Esteban, F. M., Rebassa-Mansergas, A., & Solano, E. 2022, *MNRAS*, **511**, 5462
- Tremblay, P. E., Cukanovaite, E., Gentile Fusillo, N. P., Cunningham, T., & Hollands, M. A. 2019, *MNRAS*, **482**, 5222
- Tremblay, P. E., Hollands, M. A., Gentile Fusillo, N. P., et al. 2020, *MNRAS*, **497**, 130
- van der Walt, S., Colbert, S. C., & Varoquaux, G. 2011, *CSE*, **13**, 22
- Van Winckel, H., Waelkens, C., & Waters, L. B. F. M. 1995, *A&A*, **293**, L25
- Virtanen, P., Gommers, R., Oliphant, T. E., et al. 2020, *NatMe*, **17**, 261
- Vos, J., Østensen, R. H., Marchant, P., & Van Winckel, H. 2015, *A&A*, **579**, A49
- Waelkens, C., Waters, L. B. F. M., de Graauw, M. S., et al. 1996, *A&A*, **315**, L245
- York, D. G., Adelman, J., Anderson, J. E. J., et al. 2000, *AJ*, **120**, 1579